Solar Physics (2006) 234: 135–150
DOI: 10.1007/s11207-006-0054-0

AUTOMATED DETECTION OF EUV PROMINENCES

C. FOULLON* and E. VERWICHTE
*Department of Physics, University of Warwick, Coventry CV4 7AL, UK; *Present address: Mullard Space Science Laboratory, University College London, Holmbury St Mary, RH5 6NT, UK*
(e-mail: cf2@mssl.ucl.ac.uk)

(Received 23 August 2005; accepted 5 December 2005)

Abstract. We present methods to detect automatically off-limb prominences in the extreme ultraviolet (EUV), using synoptic images taken by the extreme-ultraviolet imaging telescope (EIT) on board SOHO. The 304 Å line is essential for the detection of EUV prominences, but the optimal detection is achieved through a combined image processing of the four synoptic EIT images. In addition, the difference between consecutive 304 Å images serves to identify erupted prominences. Representation maps of the quiescent EUV prominences for a given Carrington rotation are generated and used for further analysis of the detected structures. Longitudinal profiles of long-lived prominences are investigated for three examples at different latitudes, in conjunction with on-disk intensity profiles in the EUV. The observations coincide with theoretically predicted apparent longitudinal profiles, which can be distinguished from the profile of a prominence rising before eruption. The developed algorithms may be relevant to study the 3D geometry of features seen in the EUV and may facilitate the analysis of data from the future STEREO mission.

1. Introduction

Solar filaments or prominences, which have been extensively studied in the Hα (H I) line, are associated with coronal cavities visible at wavelengths covering a wide frequency band from radio waves to soft X-rays (e.g. Vaiana, Krieger, and Timothy, 1973; Serio *et al.*, 1978; McCabe and Mickey, 1981 and references therein). Filaments, prominences and cavities form a complete ensemble of the same phenomenon. Low contrast filaments, undetected on the disk in Hα, may become visible off-limb as prominences. Moreover, part of the filament or prominence material may be too hot to emit Hα radiation while it is observed in the EUV lines (e.g. Wang *et al.*, 1998; Heinzel, Schmieder, and Tziotziou, 2001; Schmieder, Tziotziou, and Heinzel, 2003; Chae, 2003; Stellmacher, Wiehr, and Dammasch, 2003) and microwaves, the latter which, as a result, led Gopalswamy *et al.* (2003) to revisit the rate of associations between prominence eruptions and coronal mass ejections (CMEs). Furthermore, where filaments are no longer visible on the disk in Hα, associated coronal cavities persist, so that there is not necessarily a one-to-one correspondence.

Solar filaments or prominences are well known for undergoing ceaseless change in shape, being often associated with oscillations, mass flow and in extreme cases, with formation and eruption. However, they do not show significant drift over one

rotation: they form, reform and are suspended above long-lived magnetic channels in the chromosphere, apparently trapped in the overlying magnetic fields. As such, they are reliable markers of magnetic neutral lines (i.e., lines of polarity reversal of the large scale solar magnetic fields) and reveal important clues about the global field structure (see Rust, 2000 for an in-depth discussion). The large-scale polarity patterns of magnetic fields appear typically in Hα synoptic charts from Heliosynoptics, which are compiled from filaments and various fine structures in Hα images (McIntosh, 1972, 2003). Carrington maps, which are symbolic representation of both short-term and long-term solar activity (leaving out dynamical details), are particularly appropriate for long-term solar cycle studies. The use of Carrington maps, providing measurements such as rotational rates and meridional drifts of filaments, have led to a number of important findings (see e.g., Ribes, Mein, and Mangeney, 1985; Mouradian *et al.*, 1987; McIntosh, 1992, 2003; Mouradian, 1998a). These long-term solar cycle studies are solely based on information collected from on-disk observations.

However, off-limb observations are not only complementary to the on-disk observations, they provide a third spatial dimension, in the radial direction. Few long-term studies exist. Taking yearly averages of the area and height of the polar crown prominences (observed from the ground), Makarov (1994) and Makarov and Filippov (2003) showed that the polar crown prominences are becoming lower by a factor of two during their march to the poles. These studies are relevant for understanding the evolution of the global magnetic field through the solar cycles (Filippov *et al.*, 2004). For short-term studies, the prominence height may be used as a criterion for eruption, as proposed by Filippov and Den (2001) in a study of off-limb Hα prominences. This criterion may be related to prominence mass loading models (see Fong, Low, and Fan, 2002; Low, Fong, and Fan, 2003 and references therein), which require information about the plasma distribution in the corona (e.g. prominence mass or coronal cavity). The total mass of a quiescent prominence is significant for understanding, at the time of its eruption, the rise, the acceleration and the source of mass of the associated CME.

Space-based observatories offer a wealth of reliable, non-interrupted and high-cadence data, which need to be interpreted in a systematic way. In particular, an automated analysis procedure is of interest to deliver more elaborated products, ready-made for model input, long-term studies and the daily monitoring of space weather. We propose to use the synoptic images of the Sun taken by the extreme-ultraviolet imaging telescope (EIT) (Delaboudinière *et al.*, 1995, 1997; Moses *et al.*, 1997) on board the Solar and Heliospheric Observatory (SOHO). These data offer practical advantages for the detection of prominences due to their multiwavelength and full Sun resolution in the EUV and multiple interests due to their long-term archive and real-time availability. Our objective is to detect off-limb prominences in an automated way for a given Carrington rotation and to construct representations of the EUV prominences as seen by EIT in the form of Carrington maps, which

can be used for further analysis of the detected structures. The detection and the results are presented in turn.

2. Detection

The four synoptic (full disk) EIT images are taken every 6 h, at one transition region (taken at the wavelength of 304 Å) and three coronal temperatures (taken at the wavelengths of 171, 195 and 284 Å), and within a time interval of 20 min. Off-limb, the prominence is opaque in the three coronal images, seen in absorption, while in the transition region image, the prominence appears bright on the dark background of the outer space (see Moses *et al.*, 1997, p. 576, and references therein). This basic difference is the key to the off-limb detection of the EUV prominences. On the other hand, the filaments (on disk) appear dark (seen in absorption) in all four synoptic images, which makes the on-disk detection of the EUV filaments more subtle and more challenging. See example in Figure 1. The on-disk detection of the EUV filaments is not addressed here. The off-limb region is studied separately from the on-disk region. This is done in the solar image by applying round masks centred on the disk centre.

2.1. Method of histogram segmentation

We use a basic method of detection called histogram segmentation, which consists of producing, for a given input image, a binary mask by thresholding the image using its histogram. To determine such threshold, we divide the histogram of intensity levels with respect to the most common intensity level and use the Between Variance Threshold method of Otsu (1979) on one of the two parts, as follows.

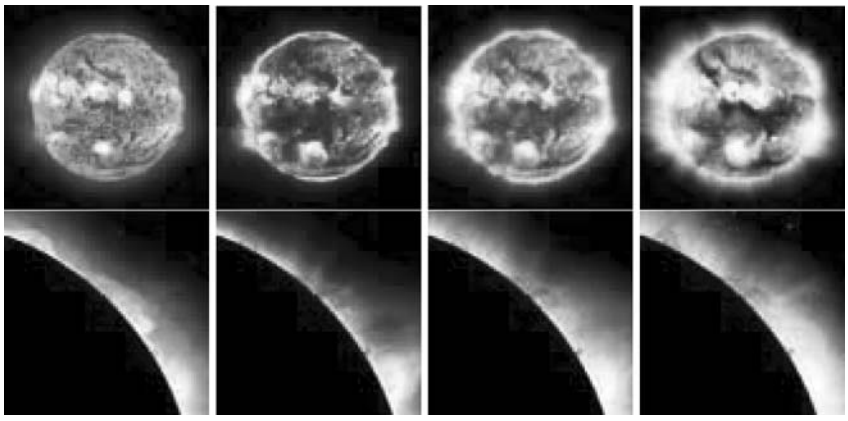

Figure 1. (*Upper*) Set of synoptic EIT images on 13 September, 1999 around 13 UT, taken at the wavelengths of 304, 171, 195 and 284 Å (respectively at 13:19, 13:00, 13:13 and 13:06 UT). (*Lower*) The corresponding snapshots of the off-limb Northwest corner (the on-disk area is masked).

For index i and bin size ΔI, H_i denotes the histogram giving the number of intensity values in the interval $[I_i - \frac{1}{2}\Delta I,\, I_i + \frac{1}{2}\Delta I]$ normalised by the total number of pixels in the image I. The optimal segmentation of the image into two classes (using histogram segmentation) is achieved by maximising the between-class variance σ^2 (Otsu, 1979), which may be written for index k as

$$\sigma^2(k) = \frac{\mu_0^k P_{k+1}^{N-1} - \mu_{k+1}^{N-1} P_0^k}{P_0^k P_{k+1}^{N-1}}, \tag{1}$$

where

$$P_p^q = \sum_{i=p}^{q} H_i \quad \text{and} \quad \mu_p^q = \sum_{i=p}^{q} i\, H_i \tag{2}$$

are respectively the probability and the average of a class of intensity values in the interval $[I_p, I_q]$.

We define the 'bright' histogram segmentation, denoted by H_{B}, the method where the Otsu threshold is applied on the right side of the histogram, with respect to the most common intensity level, and where the brightest tail in the histogram is selected. This method is illustrated further in this section, in Figure 2. Inversely, we may define the 'dark' histogram segmentation, denoted by H_{D}, the method where the Otsu threshold is applied on the left side and where the darkest tail in the histogram is selected. This latter method will not be used here.

2.2. The off-limb detection of EUV prominences

In the transition region image, taken at the wavelength of 304 Å, an off-limb prominence appears bright on the dark background. In the three coronal images, the opaque feature stands out darkly with respect to a bright active region behind it. Several methods to automatically detect the EUV prominences are initiated based on this basic property. In all methods, the reference image chosen for revealing prominences is the 304 Å image. Within the 304 Å bandpass, the He II line emits at 0.08 MK and dominates on disk, while the Si XI line, sensitive to temperatures at 1.6 MK, is significant in active regions and dominates off-limb. Active regions in this image are therefore visible because of the presence of the Si XI line. The other three coronal images serve to distinguish prominences from active regions. Thus, by taking the ratio between the 304 and 195 Å images, prominences are seen as the brightest regions and are detected as such; see Figure 3a. The enhanced prominence edges are also better detected in this ratio, where active regions appear relatively dark.

But variations in the coronal atmosphere intensity, around the solar disk, makes the detection based on a simple histogram segmentation technique unstable; see Figure 3b. To remedy to this problem, the binary image P of the detected prominences is a compilation of features detected by more than one technique, so as to

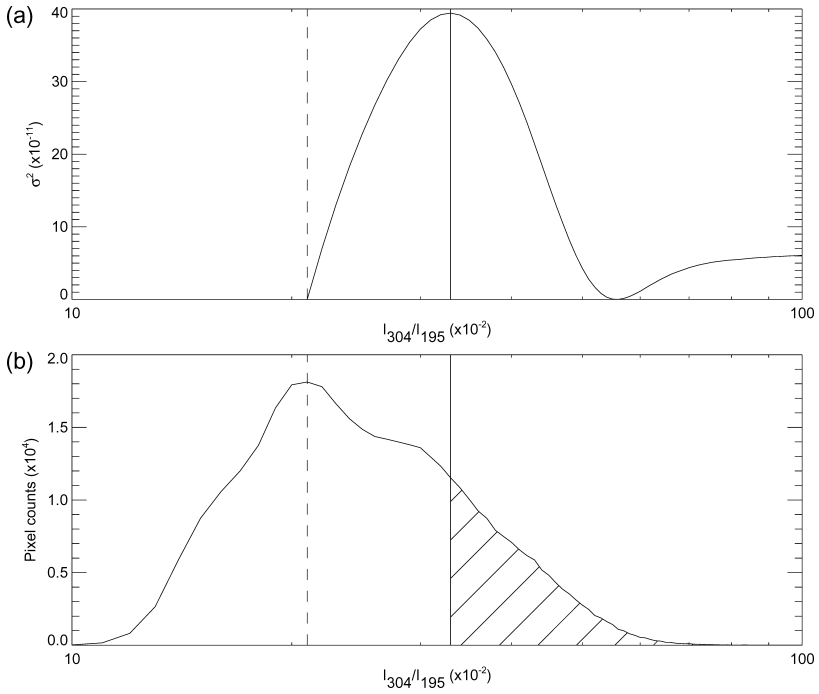

Figure 2. Illustration of H_{B}, the 'bright' histogram segmentation. (a) Between-class variance σ^2 for right part of (b) the histogram H of the solar off-limb atmosphere shown in Figure 3a. The bin size is $\Delta I = 10^{-2}$; the *vertical dashed line* indicates the peak value in H, i.e. the most common intensity level, which separates H in two parts; for the right part, the *solid vertical line* indicates the maximum between-class variance chosen as an optimum threshold value; the *hatched region* in H corresponds to 'bright' pixel values, whose positions are indicated in Figure 3b.

eliminate spurious detections arising from one or another method. We use a disk-centred ring-shaped mask, which has an inner radius at the solar limb and an outer radius touching the edges of the field of view. In addition to the bright histogram segmentation (with results shown in Figure 3c), edge detection techniques are applied (Figure 3d), as well as a more custom-build method. In this last method, the mask is divided into concentric rings or radial segments. The intensities in a 304 Å image and a coronal image are compared, within each sub-area, with the respective median values. Points of interest are then detected as the intersection of bright 304 Å and dark coronal pixels (Figure 3e–h). The different detections (Figure 3d–h) are added up. Limb regions, visible in the 304 Å image, are removed. A first binary image is compiled from points that are detected at least twice; unwanted 'salt' is removed from this image, using a morphological opening operation. The final binary image, shown in Figure 3i, is obtained by retaining only those pixels that are connected neighbours to points detected at least four times (out of a maximum of five detections).

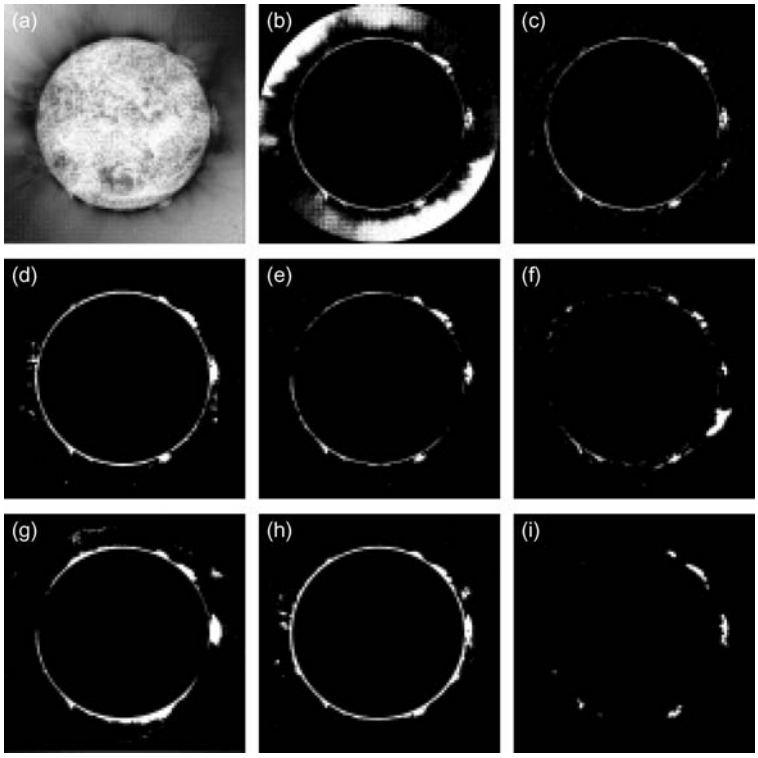

Figure 3. (a) The ratio between the 304 and 195 Å images shown in Figure 1. (b) H_B of image (a) within a disk-centred ring-shaped mask, which has an inner radius at the solar limb and an outer radius touching the edges of the field of view; the same mask is used in the following detections. (c) H_B on detected points in image (b) with their corresponding 304 Å intensities. (d) Edge detection results for the ratio image (a) combined with results (c), followed by H_B with respect to 304 Å intensities and a morphological closing operation. (e, f, g) Intersection of points detected as bright in the 304 Å image and as dark in a coronal image with respect to the medians of concentric rings; the coronal image is taken at the wavelength of (e) 195 Å, (f) 171 Å and (g) 284 Å. (h) Intersection of points detected as bright in the 304 Å image and as dark in 284 Å image with respect to the medians of radial segments. (i) The detected off-limb prominences (P).

2.3. ERUPTED PROMINENCES

It happens that some of the detected prominences are erupting material (i.e. not visible in the previous or next 304 Å image). To identify those erupted prominences, the difference between consecutive 304 Å images is used. Figure 4 illustrates the method for a prominence erupting in the North West corner and corresponding to one of the prominences seen before the eruption in the lower panel of Figure 1. This method deals only with prominences erupting close to the limb, within a ring-shaped mask (as shown in Figure 4b). Any feature detected in the difference between consecutive 304 Å images is compared with off-limb features P from the

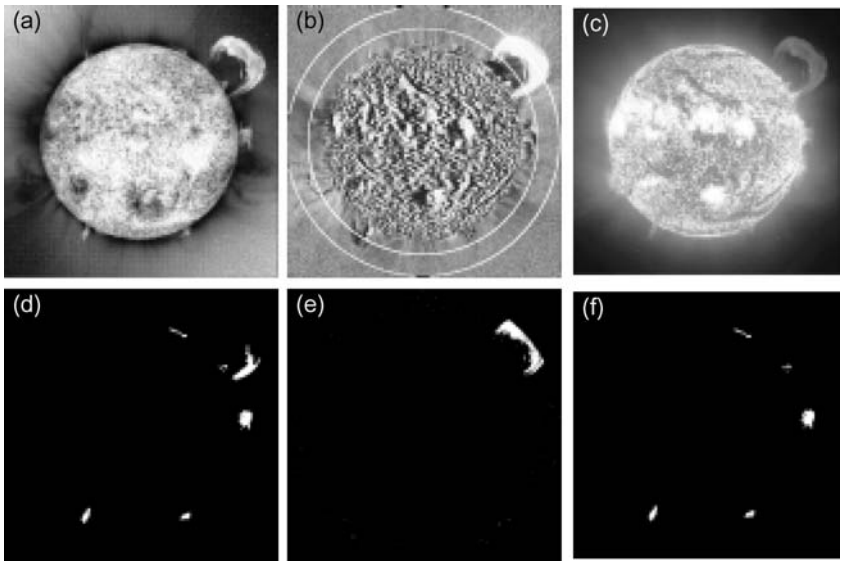

Figure 4. Final processing illustrated for the EIT 304 Å full-disk solar image taken at 7:19 UT on 14 September, 1999. (a) The ratio between the 304 and 195 Å images in the same synoptic set. (b) Difference between the 304 Å image and an earlier 304 Å image (taken at 01:19 UT). The *white circles* superimposed represent the edges of a disk-centred ring-shaped mask, which has an inner radius above the solar limb and an outer radius touching the edges of the field of view. (c) The 304 Å image. (d) The detected off-limb prominences following the general procedure. (e) H_B of image (b) within the ring-shaped mask. (f) The final detected off-limb prominences P, after removing the erupted material from (d).

general procedure. If common pixels are found, the pixels in P that are connected neighbours to the common pixels are removed.

Table I gives characteristic details of the erupted material, which are generated automatically by applying the detection algorithm to EIT synoptic data sets to be found in 1999 between August 9, 19 UT and September 23, 23 UT (corresponding to Carrington rotation (CR) $\pm 90^\circ$, for reasons explained later). The information extracted is helpful to identify the origin of the eruptions and their direction of propagation, which may be compared to their subsequent evolution in coronagraph data (e.g. using the central position angle and angular width available in the CME catalogue compiled from observations by the large angle and spectrometric coronagraph experiment, LASCO). For completeness, the present method could be extended to detect all erupting material appearing in 304 Å images (i.e. including material high above the limb). However, this is beyond the scope of our investigation.

3. Results

We now examine the detected off-limb prominences in more detail. Of the four EIT wavelengths, the 304 Å line was shown to be essential for their detection. However,

TABLE I

Erupted prominences close to the limb, captured in 304 Å by EIT.

Date	Time	l	CR	L	ΔL	B	ΔB	PA	AW
99/08/17	07:19:07	E	1953	292.06	6.30	−55.35	15.65	146.0	16
99/08/20	19:18:53	W	1952	78.98	13.15	73.13	8.19	344.5	9
99/09/04	19:19:11	E	1953	38.57	2.00	−12.33	14.84	102.5	15
99/09/08	13:19:08	W	1953	162.36	1.95	−31.14	10.90	238.5	11
99/09/14	01:19:10	E	1954	285.80	4.08	−55.29	9.76	146.0	10
99/09/14	07:19:07	W	1953	95.12	1.98	29.73	11.90	300.0	12
99/09/17	13:19:08	E	1954	226.27	0.82	17.84	5.94	72.0	6

The erupted material is described by the date and time of the 304 Å EIT image, the limb l of observation (East or West), the off-limb positions in Carrington rotation CR (mean Carrington longitude L, longitudinal extent ΔL, mean latitude B, latitudinal extent ΔB) and in the plane of the sky (central position angle PA measured from Solar North, counter clockwise, and angular width AW). All angles are in degrees.

in contrast to detections with one single optical wavelength, the combination of all four EIT synoptic images was necessary to reach optimal results. To assess these results, it is useful to construct the EUV Carrington maps of prominences. These maps can then be compared with other synoptic maps and can be used to further study the prominences in their longitudinal extent.

3.1. EUV CARRINGTON MAPS OF PROMINENCES

To obtain a set of images featuring the off-limb prominences P for a complete Carrington rotation (CR), one needs not only the data of the given CR but also the data to be found within 90° of Carrington longitude before or after the considered CR. This thus represents data ranging over a period of about 41 days. The detection algorithm is applied to EIT synoptic data sets to be found within Carrington rotation $1953 \pm 90°$ (99/08/09, 9 UT – 99/09/23, 23 UT).

Heliographic coordinates of the EUV prominences are then determined for each off-limb point in a given image P. The latitude and longitude of a point above the limb are taken to be the heliographic coordinates of the closest point on the limb. Each point is then positioned in a Carrington map, with separate maps for East limb prominences and West limb prominences. Grey levels are used to indicate the maximum height of prominence material observed at each location. The maps obtained for CR = 1953 are shown in Figure 5a and b. Figure 6a shows the EUV Carrington map of the East and West limb prominences together.

The limb points at a given date and time, corresponding to a set of synoptic EIT images, are aligned along curved lines. If the limb longitudes were taken to be ±90° of the Carrington longitude at the central meridian, then the lines would

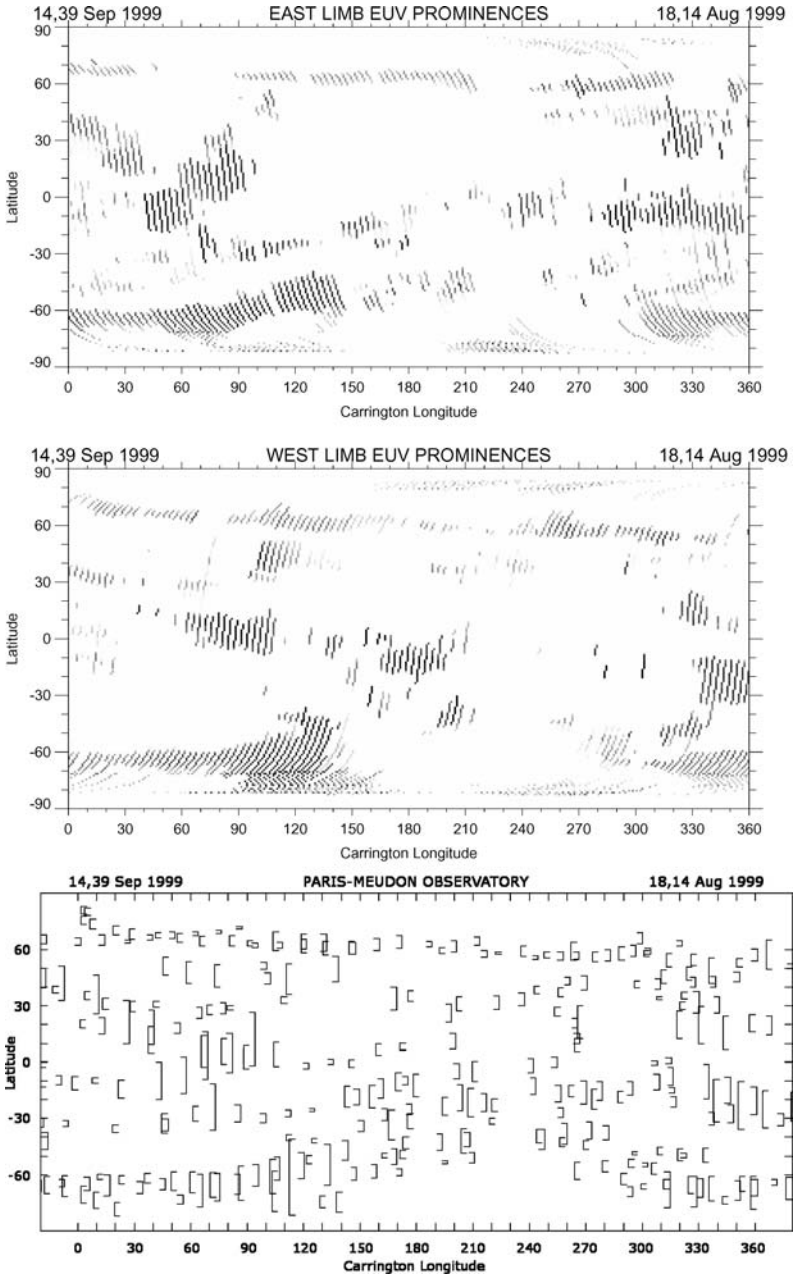

Figure 5. EUV Carrington maps of prominences observed, in Carrington rotation 1953, (a) on the East limb and (b) on the West limb; decreasing *grey levels* are used to represent increasing maximum height of prominence material. (c) For comparison, the corresponding synoptic map of prominences from the Paris-Meudon Observatory; *brackets*, orientated toward West or East according to the limb observed, indicate the longitude of the limb and the latitude extension of the prominences (determined from K3 spectroheliograms).

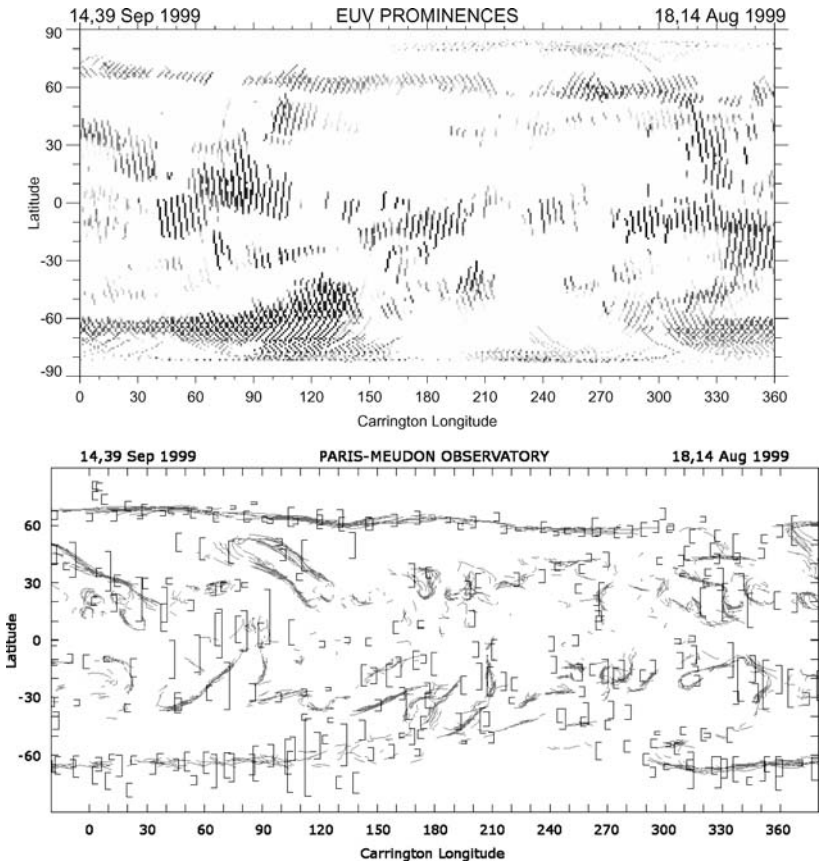

Figure 6. EUV Carrington maps of prominences observed in Carrington rotation 1953, by addition of the prominences observed on the East and West limbs; *grey levels* are used to represent increasing maximum height of prominence material (in the case of two detections at the same position, the averaged value is represented). (b) For comparison, the corresponding synoptic map of Hα filaments (©Observatoire de Paris – BASS2000).

be vertical. Here, due to the heliographic latitude of the central point of the solar disk, the tilt angle B_0, the longitudinal corrections to the vertical lines on the East limb are opposite to the corrections for the West limb. As a result, the opposite patterns seen in Figure 5a and b may be recognised in Figure 6a and may serve to identify the limb of observation of a given prominence. These opposite patterns change directions depending on the sign of B_0, which is here positive.

Results of the off-limb detection in the EUV appear to be in reasonable agreement with synoptic maps compiled from observations at optical wavelengths from the Paris-Meudon Observatory (Figures 5c and 6b). These maps show daily prominence positions observed on the limb and daily filament traces; the limb position of prominences (not corrected for B_0) are determined from K3 spectroheliograms

(Ca II, at 393.37 nm) if the latitude extension on the limb is greater than 2° or the apparent height is greater than 20 000 km, while the base-line of filaments are revealed in Hα (H I, at 656.28 nm) (Mouradian, 1998b).

Several uncertainties in the longitudinal position of prominences may contribute to differences between prominences detected off the limb and filaments on the disk. First, the true longitudinal position of the structure seen in the line-of-sight may differ from the limb longitudinal position by an extent which depends on the height of the structure. Second, the differences between the Carrington rotation and the true rotation of the filament must be taken into account. The true rotation of filaments is either differential with latitude (d'Azambuja law) or may include pivot points (see e.g. Mouradian *et al.*, 1987).

3.2. Longitudinal profiles of EUV prominences

The EUV Carrington maps of prominences can be used to further study the prominences in their longitudinal extent. For illustration, we examine a region on the Sun located in a 90°-wide quadrant ($B = S5°$–$N85°$, $L = 60°$–$150°$). The map of prominences for this region is shown in Figure 7, next to the corresponding heliographic projection of the disk observed by EIT in the 195 Å bandpass (obtained with a spatial resolution of two pixels per degree). Three areas of interest with distinct latitudes are studied. The high-latitude area contains a polar crown filament, stretched in the direction of solar rotation (parallel to the solar equator). The mid-latitude area shows a pair of long and inclined parallel filaments, adjoining a

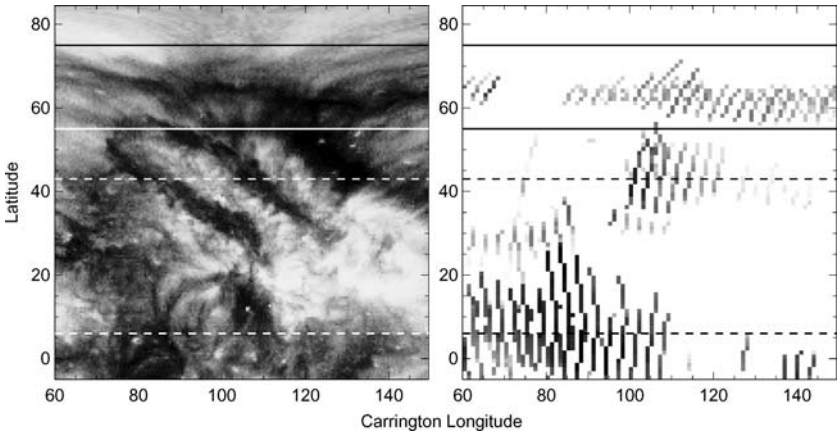

Figure 7. Region of the Sun in Carrington rotation 1953 ($B = S5°$–$N85°$, $L = 60°$–$150°$): (*left*) heliographic projection of the 195 Å EIT full-disk solar image taken on 6 September 1999 at 6:36 UT (with central meridian at $L = 107.3°$) and (*right*) map of the EUV prominences. The upper section shown within *solid lines* contains a polar crown filament. Longitudinal profiles at mid-latitude and near the solar equator are indicated by *dashed lines*.

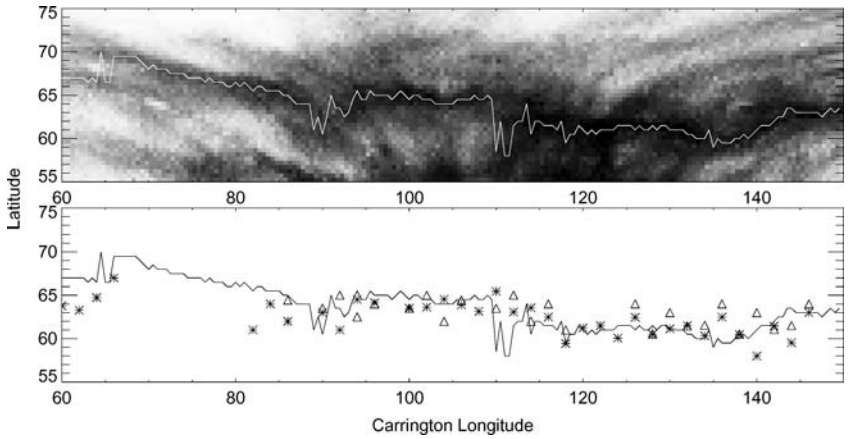

Figure 8. (*Top*) Heliographic map ($B = 55^\circ$–75°, $L = 60^\circ$–150°) of polar crown EUV filament and (*bottom*) corresponding weighted-average positions of EUV prominences observed on the East and West limbs, shown with *triangle* and *star* symbols respectively. The *solid curve* indicates the positions where the 195 Å intensity reaches a local minimum (in a 1.5°-boxcar running average of each latitudinal profile).

coronal hole on the West of them. Below the filaments, in the lower area, a small equatorial coronal hole is located West of a wide prominence cloud. The coronal holes can be observed in He I (1083 nm) from the Kitt Peak (KP) station of the National Solar Observatories (NSO), referring to the NSO/KP Carrington map or to the Heliosynoptics chart (McIntosh, 2003, Figure 7).

We first consider the polar crown prominence. For each longitude, we obtain the average latitude B, weighted with the prominence height, *viz.*

$$B = \frac{\sum_j h_j B_j}{\sum_j h_j}, \tag{3}$$

where h_j is the apparent height of a prominence at latitude B_j. The resulting positions, shown in Figure 8, correlate well with positions along the path of lowest intensity in the polar crown EUV filament channel, despite the uncertainties in the true off-limb prominence positions.

To explain the longitudinal profiles of prominences, we next consider a model for the apparent height of a prominence sheet of thin longitudinal extent rotating and visible off the limb, as seen from the Earth. For a sheet of height h_0 located at longitude L_0, its apparent height h above the solar limb of longitude L is given by

$$\frac{h(L)}{R_\odot} = \left(\frac{h_0}{R_\odot} + 1\right)\cos(L - L_0) - 1, \qquad L_0 - \frac{\Delta L}{2} \le L \le L_0 + \frac{\Delta L}{2}, \tag{4}$$

where ΔL is the apparent longitudinal extent of the prominence sheet, given by

$$\cos\left(\frac{\Delta L}{2}\right) = \left(\frac{h_0}{R_\odot} + 1\right)^{-1}. \tag{5}$$

The best cases where this simple model of apparent height can be applied and verified are the low and mid-latitude prominences, which have structural changes in the longitudinal direction. Longitudinal profiles of prominences, taken at 6° and 43° of latitude, respectively, are studied in conjunction with intensity profiles in the EUV showing filaments and coronal holes on the disk. The profiles in the EUV are obtained by averaging 195 Å intensities over one degree of latitude (i.e. two pixels); see Figures 9 and 10. For the East and West limbs, respectively, h_0 is taken to be the maximum observed apparent height along the prominence profile and L_0 corresponds to the longitude of lowest intensity in a filament channel. Equations (4) and (5) are then applied to see if the longitudinal profiles of prominences can be understood in terms of apparent longitudinal profiles.

The prominence near the equator, studied in Figure 9, features such a profile. Therefore, in this case, the apparent detection of prominence material at the location of a coronal hole on the disk can be explained by the tip of the prominence turning on the limb, and not necessarily by differences between the Carrington rotation and the true rotation of the filament.

The pair of filaments at mid-latitude, studied in Figure 10, erupt as prominences over the West limb on 14 September, 1999 (as seen in 195 Å high-cadence

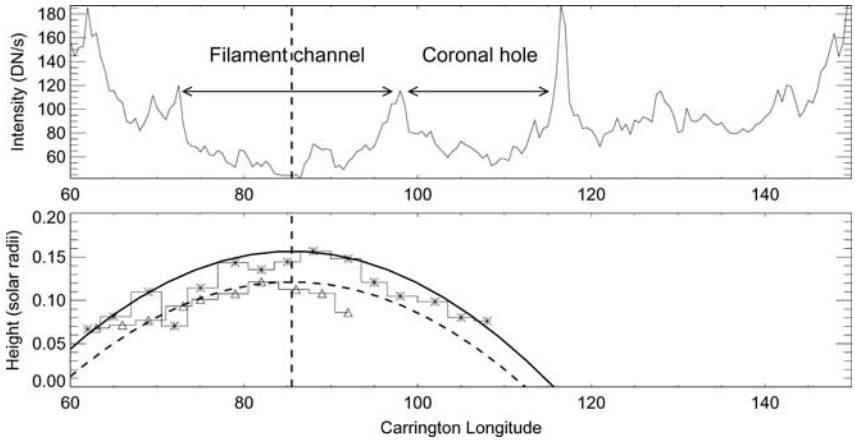

Figure 9. Longitudinal profiles at $B = 6°$: (*top*) 195 Å intensity showing a filament channel and an equatorial coronal hole on the disk and (*bottom*) apparent heights of prominences observed on the East and West limbs, shown with *triangle* and *star* symbols, respectively. For the respective limbs, the *dashed* and *solid curves* indicate the theoretically predicted apparent height of a prominence sheet of thin longitudinal extent rotating and visible off the limb; the height of the sheet is taken to be the maximum observed apparent height and its location is where the intensity (in a 2.5°-boxcar running average) reaches a local minimum, as indicated by the *vertical dashed* line.

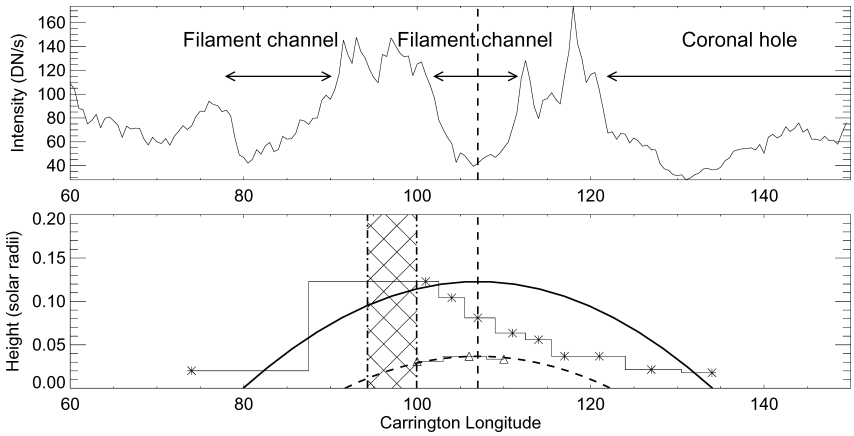

Figure 10. Longitudinal profiles at $B = 43°$: (*top*) 195 Å intensity showing a coronal hole and the channels of two inclined parallel filaments and (*bottom*) apparent heights of prominences observed on the East and West limbs. *Lines*, *curves* and *symbols* are as in Figure 9. The *hatched region* represents the longitudinal position and extent of the erupted prominence shown in Figure 4e.

images), resulting in CME material being ejected. The 304 Å image shown in Figure 4 captures the eruption of the Northern prominence, at 07:13 UT; the second prominence to the South–East starts to erupt near 08:00 UT. Figure 10 shows how the rise of the Northern prominence, before its eruption, differ markedly from a theoretically predicted apparent height profile. In principle, it is possible to distinguish the changes due solely to the rise from the apparent height. While the longitudinal profile on the East limb fits the predicted apparent longitudinal profile, the apparent detection on the West limb of prominence material at the location of a coronal hole on the disk could signify that the prominence sheet is of thick longitudinal extent, which should be taken into account to predict the apparent height more accurately. Such observation and analysis can be useful for understanding the factors leading to the eruptions. It is interesting to note that, following the filament in the 195 Å high-cadence images as it crossed the solar disk led to the discovery of ultra-long-period oscillations in the filament (Foullon, Verwichte, and Nakariakov, 2004), which were suggested to play a role for explaining the eruptions.

4. Conclusions

The automated detection of prominences off-limb in the EUV is achieved through a combined image processing of the four synoptic EIT images. Using the results of the detection, we have shown that it is possible to construct Carrington maps of long-lived and quiescent structures as seen by EIT, which are in reasonable

agreement with synoptic maps compiled from observations at optical wavelengths. Through an investigation of three examples at different latitudes, we have studied the correlations between prominences and filaments seen in the EUV and showed that longitudinal profiles of prominences coincide with theoretically predicted apparent longitudinal profiles, which can be distinguished from the profile of a prominence rising before eruption.

Broad EUV extensions of Hα filaments on the disk have been interpreted by Aulanier and Schmieder (2002) and by Schwartz *et al.* (2004) as a result of low-lying structures and high-altitude cold clouds surrounding Hα filaments, respectively. The height and the longitudinal extent of the EUV prominences might be used in conjunction with the geometry of on-disk filaments to understand the physical nature of both features seen in the EUV. Ultimately, the two sets of observations might be used to estimate the volume and, for a suitable density model, a realistic approximation of the prominence mass. An automated detection of EUV filaments on the disk would be desirable. However, the confusion in the EUV between filaments and other structures on the disk (i.e. dark quiet Sun and coronal hole regions) would require a separate investigation and, presumably, highly sophisticated methods.

The work presented here is the first step towards future case studies of important events and towards extracting statistical properties over longer periods, which, given the size of the present EIT archive ranging over nearly a solar cycle, could provide valuable and complementary studies to the Hα filament studies. The present efforts to detect EUV prominences in EIT images are also expected to facilitate the analysis of data from future EUV instruments, in particular those with bandpasses identical as those with EIT, such as the EUVI/SECCHI instruments on board the twin STEREO spacecrafts (Howard *et al.*, 2002). In this latter case, the detection will be possible from two simultaneous views. This will add precision and better resolution to the spatial distribution of the prominence material, represented in the form of Carrington maps. Two perpendicular simultaneous views in the four wavelengths from the EUVI instruments will also provide an 'exact' (as opposed to delayed) comparison between filaments and prominences seen in the EUV.

Acknowledgements

C.F. gratefully acknowledges the hospitality and support from the Space and Astrophysics Group at the University of Warwick. We would like to express our gratitude to the referee G. Aulanier and the Editor L. van Driel-Gesztelyi for their constructive comments and encouragements. This work was partly funded by the ESA/PRODEX project under contract 14815/00/ NL/SFe(IC), The Solar Drivers of Space Weather. EIT data are courtesy of SOHO/EIT consortium. SOHO is a project of international cooperation between ESA and NASA.

References

Aulanier, G. and Schmieder, B.: 2002, *Astron. Astrophys.* **386**, 1106.

Chae, J.: 2003, *Astrophys. J.* **584**, 1084.

Delaboudinière, J. -P., Artzner, G. E., Brunaud, J., Gabriel, A. H., Hochedez, J. F., Millier, F., *et al.*: 1995, *Solar Phys.* **162**, 291.

Delaboudinière, J. -P., Stern, R. A., Maucherat, A., Portier-Fozzani, F., Neupert, W. M., Gurman, J. B., *et al.*: 1997, *Adv. Space Res.* **20**, 2231.

Filippov, B. P. and Den, O. G.: 2001, *J. Geophys. Res.* **106**, 25177.

Filippov, B. P., Platov, Y. V., Ajabshirizadeh, A., and Klepikov, D. V.: 2004, *Solar Phys.* **224**, 277.

Fong, B., Low, B. C., and Fan, Y.: 2002, *Astrophys. J.* **571**, 987.

Foullon, C., Verwichte, E., and Nakariakov, V. M.: 2004, *Astron. Astrophys.* **427**, L5.

Gopalswamy, N., Shimojo, M., Lu, W., Yashiro, S., Shibasaki, K., and Howard, R. A.: 2003, *Astrophys. J.* **586**, 562.

Heinzel, P., Schmieder, B., and Tziotziou, K.: 2001, *Astrophys. J.* **561**, L223.

Howard, R. A., Moses, J. D., Socker, D. G., Dere, K. P., and Cook, J. W.: 2002, *Adv. Space Res.* **29**, 2017.

Low, B. C., Fong, B., and Fan, Y.: 2003, *Astrophys. J.* **594**, 1060.

Makarov, V. I.: 1994, *Solar Phys.* **150**, 359.

Makarov, V. I. and Filippov, B. P.: 2003, *Solar Phys.* **214**, 55.

McCabe, M. K. and Mickey, D. L.: 1981, *Solar Phys.* **73**, 59.

McIntosh, P. S.: 1972, in P. S. McIntosh and M. Dryer (eds.), *Progress in Astronautics and Aeronautics*, Vol. 30. MIT Press, Cambridge, p. 65.

McIntosh, P. S.: 1992, The Solar Cycle, *ASP Conference Series* **27**, 14.

McIntosh, P. S.: 2003, Solar Variability as an Input to the Earth's Environment, *ESA SP* **535**, 807.

Moses, D., Clette, F., Delaboudinière, J.-P., Artzner, G. E., Bougnet, M., Brunaud, J., *et al.*: 1997, *Solar Phys.* **175**, 571.

Mouradian, Z.: 1998a, Synoptic Solar Physics, *ASP Conference Series* **140**, 181.

Mouradian, Z.: 1998b, Synoptic Solar Physics, *ASP Conference Series* **140**, 197.

Mouradian, Z., Martres, M. J., Soru-Escaut, I., and Gesztelyi, L.: 1987, *Astron. Astrophys.* **183**, 129.

Otsu, N.: 1979, *IEEE Trans. Syst. Man Cyber.* **9**(1), 62.

Ribes, E., Mein, P., and Mangeney, A.: 1985, *Nature* **318**, 170.

Rust, D. M.: 2000, *J. Astrophys. Astron.* **21**, 177.

Schmieder, B., Tziotziou, K., and Heinzel, P.: 2003, *Astron. Astrophys.* **401**, 361.

Schwartz, P., Heinzel, P., Anzer, U., and Schmieder, B.: 2004, *Astron. Astrophys.* **421**, 323.

Serio, S., Vaiana, G. S., Godoli, G., Motta, S., Pirronello, V., and Zappala, R. A.: 1978, *Solar Phys.* **59**, 65.

Stellmacher, G., Wiehr, E., and Dammasch, I. E.: 2003, *Solar Phys.* **217**, 133.

Vaiana, G. S., Krieger, A. S., and Timothy, A. F.: 1973, *Solar Phys.* **32**, 81.

Wang, H., Chae, J., Gurman, J. B., and Kucera, T. A.: 1998, *Solar Phys.* **183**, 91.